Correlating corrosion to surface grain orientations of polycrystalline aluminum alloy by scanning electrochemical cell microscopy

Li, Yuanjiao; Morel, Alban; Gallant, Danick; Mauzeroll, Janine

Publisher's version / Version de l'éditeur:
https://doi.org/10.1021/acsami.2c12813
ACS Applied Materials & Interfaces, 14, 41, pp. 47230-47236, 2022-10-07

ACS APPLIED MATERIALS & INTERFACES

www.acsami.org

Research Article

Correlating Corrosion to Surface Grain Orientations of Polycrystalline Aluminum Alloy by Scanning Electrochemical Cell Microscopy

Yuanjiao Li, Alban Morel,* Danick Gallant,* and Janine Mauzeroll*

Cite This: *ACS Appl. Mater. Interfaces* 2022, 14, 47230–47236

Read Online

ACCESS | Metrics & More | Article Recommendations | Supporting Information

ABSTRACT: The study of grain-dependent corrosion behaviors of practical polycrystalline metals remains challenging due to the difficulty in eliminating the influences of other microstructural features, such as intermetallic particles and grain boundaries. In this work, we performed thousands of microscopic potentiodynamic polarization measurements on a polycrystalline aluminum alloy AA7075-T73 using the spatially resolved oil-immersed scanning electrochemical cell microscopy measurement. Data were extracted only from grain interior areas excluding intermetallic particles and grain boundaries. Based on the multiple potentiodynamic polarization measurements, the differences between grains can be revealed. Cathodic currents exhibited a strong grain orientation dependence with a decreasing order of {101} > {001} > {111}, agreeing with the prediction from the order of atomic planar density. By contrast, the dependence of anodic currents on grain orientation was weak, and pitting was independent of grain orientation, which could be due to the limited mass transport of ions within the surface oxide film. This work highlights the capability of oil-immersed scanning electrochemical cell microscopy in resolving small electrochemical differences, which will greatly promote the study of grain-dependent behaviors of practical polycrystalline samples.

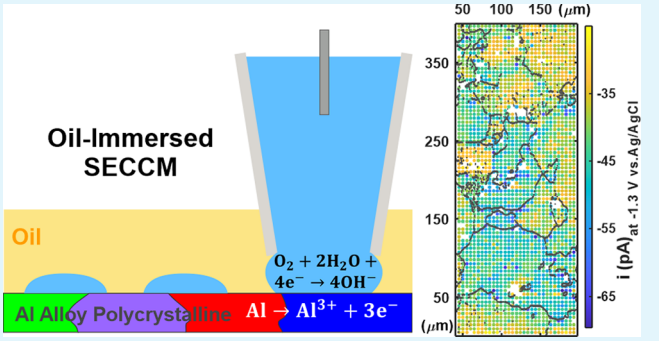

KEYWORDS: *scanning electrochemical cell microscopy (SECCM), grain orientation, corrosion, polycrystalline, Al alloy*

1. INTRODUCTION

Alloys are composed of numerous grains in different sizes and orientations with grain boundaries between them, which are critical in determining the properties of materials. The crystallographic orientations of grains influence the growth of oxide film,[1,2] surface treatment,[3,4] and tensile strength.[5,6] However, the effect of grain orientations on corrosion behaviors is still poorly understood.[7−11] Most previous studies were performed on single crystals to eliminate the influence of intermetallic particles and grain boundaries,[12−16] which are nevertheless not realistic for practical applications. However, there lacks a scanning electrochemical technique that enables direct microscopic corrosion measurements on individual grains of polycrystalline samples.

The emergence of single-channel pipette scanning electrochemical cell microscopy (SECCM)[17] and the following double-channel pipette SECCM[18] opens up the prospect of spatially resolved measurements of corrosion-related electrochemical processes. In SECCM, a droplet cell is created at the end of an electrolyte-filled micropipette used to scan the substrate surface and perform microscopic electrochemical measurements. SECCM maps can reveal the electrochemical differences correlated to the surface structural heterogeneity.

In 2019, Yule et al. performed SECCM on low carbon steel, revealing the dependence of anodic passive films on grain orientations based on the comparison between potentiodynamic polarization (PDP) curves.[19] However, the limited number of measurements cannot provide more specific information. A larger number of measurements is required on more grains. This can be realized by performing short-time measurements at each droplet landing,[20−22] but is not applicable for the time-consuming open circuit potential (OCP) and PDP measurements of corrosion in neutral solutions. Moreover, because grain orientations are randomly distributed, a large surface area needs to be mapped to include diverse grain orientations. This necessitates a highly stable droplet cell capable of long-term scanning. In 2020, oil-immersed SECCM (OI-SECCM) was developed, in which the

Received: July 18, 2022
Accepted: September 20, 2022
Published: October 7, 2022

droplet was immersed under a thin layer of hydrophobic and inert oil on the substrate surface.[23,24] This prevents the droplet from evaporating and spreading, which significantly increases the stability of the droplet electrochemical cell.[22,23,25]

Taking advantage of OI-SECCM, this work explored the correlation between corrosion and grain orientations of Al alloy AA7075-T73. For Al, the presence of a passive oxide film reduces the conductivity and reactivity of the surface,[26,27] resulting in extremely low currents in microscopic electrochemical measurements. Low currents make it difficult to distinguish small electrochemical differences between grains. By controlling the value of approach potential of single-channel pipette SECCM applied during the micropipette approach to the substrate, the conductivity of surface oxide can be appropriately increased according to our previous work. This will damage the oxide film to a small extent but still allow the study of grain-dependent behaviors.

The PDP measurements of multiple grains revealed a clear grain orientation dependence of cathodic currents, which decreased in the order of {101} > {001} > {111} consistent with the reverse order of atomic planar density. Furthermore, the OI-SECCM maps showed enhanced cathodic activity and pitting preference at grain boundaries, reflecting the higher reactivity of grain boundaries. In contrast, anodic currents and pitting were less correlated with grain orientations. The statistical analyses based on the large number of measurements ensure the reliability of results. This will promote the study of grain-dependent electrochemical behaviors directly on polycrystalline samples.

2. EXPERIMENTAL SECTION

2.1. Chemicals and Materials. Sodium chloride (NaCl, anhydrous, 99.8%) and mineral oil (M5310) were used as purchased from Sigma-Aldrich. Quartz glass capillaries (Sutter Instrument, Novato, CA) with dimensions of (o.d./i.d.) 1.0/0.3 mm were pulled (P-2000 CO2-laser puller, Sutter Instruments, USA. to produce two single-channel micropipettes with a tip diameter of ~ 2 μm.

AA7075-T73 Al alloy was provided by National Research Council (NRC Canada, Saguenay), and the composition is listed in Table S1. A small piece of sample (~1.5 × 1.5 cm^2) was fixed in cold mounting epoxy (EpoFix, Struers). AA7075-T73 was ground using a 320 grit SiC paper (Struers, Canada) and polished using 9 μm and 3 μm colloidal diamond suspensions and finally a colloidal silica suspension (Struers, Canada) on a MD Chem cloth (Struers, Canada) to obtain a mirror-like surface. The sample surface was then rinsed using anhydrous ethanol and sonicated in ultrapure water to remove the residue of silica suspension before drying in air.

The Ag/AgCl reference electrode (RE) was made using a Ag wire (0.5 mm diameter, Goodfellow Metals, Huntingdon, England) immersed in household bleach.[25,28,29] Ag was oxidized in the bleach to form a AgCl outer coat on the wire. The potential stability and reproducibility of the Ag/AgCl electrode have been verified in our previous work,[23,25] which has a 5 mV difference with respect to SCE in 3.5 wt % NaCl solution. All potentials reported in this work have been calibrated to Ag/AgCl wire RE in 3.5 wt % NaCl solution.

All electrochemical measurements were performed using an EIProScan 3 system (HEKA, Germany; bipotentiostat model PG340) in a Faraday cage (Acoustic Isolation Novascan Ultracube, Ames, IA, USA) on a vibration isolation table (Micro 60 Halcyonics Active Vibration Isolation Platform, Novascan, Ames IA, USA).

2.2. Oil-Immersed SECCM. OI-SECCM was carried out as previously reported.[22,23,25] Briefly, a 2 μm diameter micropipette was filled with the 3.5 wt % NaCl aqueous solution, creating a droplet cell at the tip. The droplet was immersed under a layer of mineral oil on the surface of the working electrode (WE) substrate to prevent droplet evaporation. A three-electrode arrangement was used as shown in Figure 1a, where a non-isolated Ag/AgCl wire and Pt wire served as the RE and the counter electrode (CE), respectively. The distance between the end of Ag/AgCl wire and micropipette tip was extended to 50 cm with a polyvinyl chloride plastic tube (inner diameter, 0.76 mm), similar to the microcapillary cell setup,[30] but in this work, it is to eliminate the interference of Ag^+ ions from Ag/AgCl wire on electrochemical measurements.[25,31] The tube connected the micropipette to a more open syringe, where both RE and CE were immersed in the electrolyte. The more open space allows to use a commercial isolated RE in OI-SECCM experiments, although the non-isolated Ag/AgCl wire was still employed in this work to be consistent with our previous works.[23,25] The micropipette was approached to the WE under the mineral oil with an approach potential of −2.5 V applied. Upon the droplet landing on WE, the electrochemical circuit was closed giving rise to a current spike which triggered the micropipette to stop moving. Once triggered, the approach potential was removed, and OCP was measured for 30 s followed by a PDP measurement. PDP was carried out at 100 mV/s from −1.35 to −0.3 V. After that, the micropipette was retracted and laterally moved to the next location in a hopping mode with a separation of 5 μm between locations.

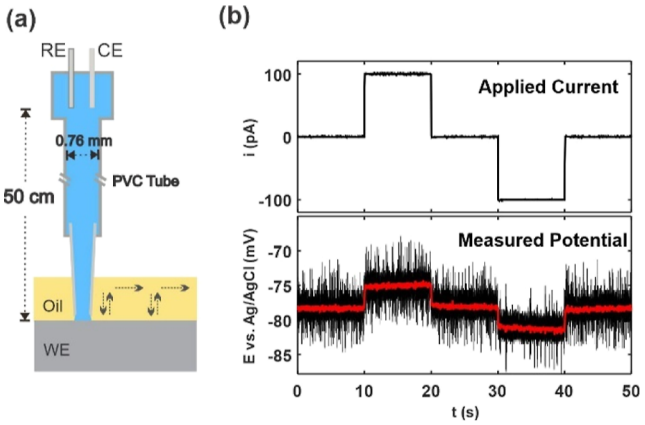

Figure 1. (a) Schematic of the OI-SECCM setup using a 41 cm long polyvinyl chloride tube (inner diameter: 0.76 mm), which extends the distance between Ag/AgCl RE and WE to 50 cm. A Pt wire serves as CE. (b) Waveforms of the potential changes in response to the applied currents. Glassy carbon was used as WE.

2.3. Surface Characterization. The Al alloy surface scanned by OI-SECCM was imaged by optical microscopy (Figure S1a) and scanning electron microscopy (SEM) (Figure S1b−d). Some corrosion product particles were left on the droplet landing surface after OCP and PDP measurements, which have a higher content of oxygen and lower content of aluminum shown in the surface energy-dispersive X-ray spectroscopy maps (Figure S1e,f). This indicates the occurrence of corrosion. Electron backscattered diffraction (EBSD) were conducted at an acceleration voltage of 20 keV with a step size of 0.7 μm. EBSD was performed with an Oxford SDD EBSD detector on a Hitachi SU3500 variable pressure scanning electron microscope. The alloy surface was tilted 70° to the EBSD detector. Inverse pole figure color maps were obtained showing the grain orientations of Al alloy. The EBSD maps and electrochemical data obtained by OI-SECCM were analyzed using MATLAB R2020a.

3. RESULTS AND DISCUSSION

3.1. iR_Ω between RE and WE. The long distance between RE and WE designed in the OI-SECCM setup (Figure 1a) eliminated the interference of RE contaminants on the electrochemical measurements of WE but could lead to a high ohmic drop (iR_Ω) between RE and WE. Our previous study[25] found that the commonly used non-isolated Ag/AgCl

https://doi.org/10.1021/acsami.2c12813
ACS Appl. Mater. Interfaces 2022, 14, 47230−47236

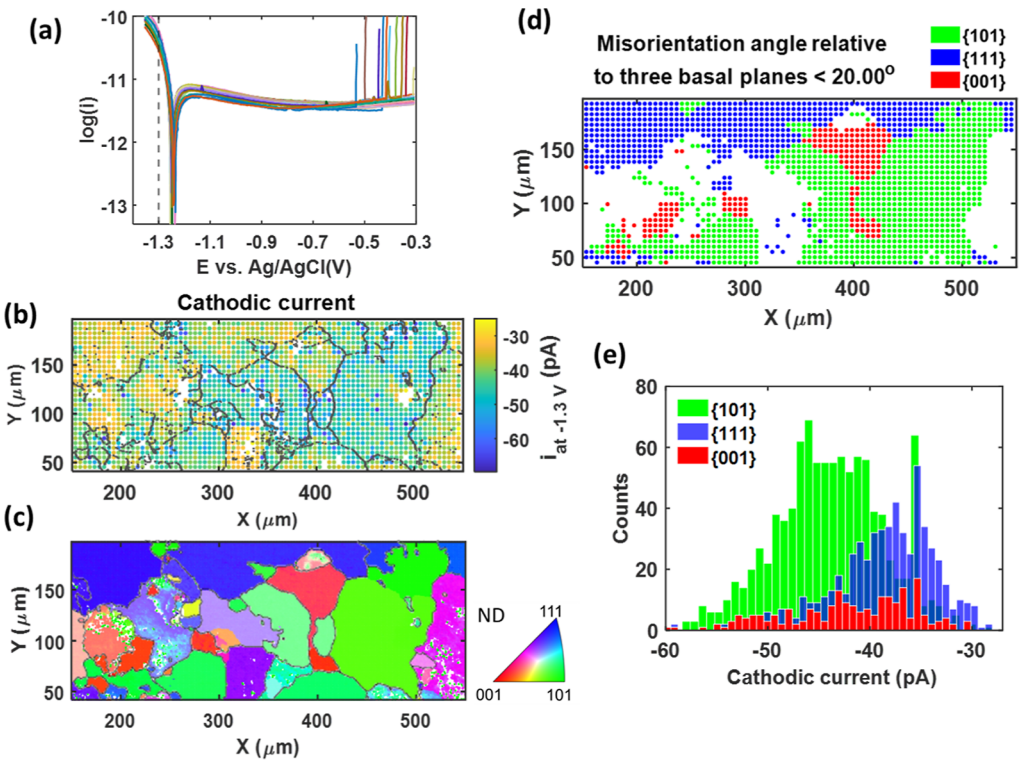

Figure 2. (a) 26 PDP curves randomly selected from the 2511 locations on OI-SECCM maps. (b) Cathodic current map superimposed on the grain boundary map, in which the cathodic currents were extracted from PDP curves at −1.3 V vs Ag/AgCl. The currents were confined between −70 and −25 pA to remove the higher currents on intermetallic particles. (c) EBSD inverse pole figure color map showing the grain orientations with respect to the sample normal direction (ND). (d) Diluted grain orientation map containing the grains with misorientation angles less than 20° relative to the {101}, {111}, and {001} planes. (e) Statistical distribution of cathodic currents (at −1.3 V vs Ag/AgCl) on the three groups of grains.

wire QRCE leaked Ag^+ into electrolyte, which diffused to the tip of micropipette in a prolonged experiment.

The reduction of interfering Ag^+ ions on WE generated a considerable cathodic current that would make the small current differences between grains undetectable. In this work, we extended the distance between Ag/AgCl wire RE and WE to 50 cm to ensure that the droplet cell is free of Ag^+ throughout the experimental time of ∼40 h. However, the extended distance may decrease the actual potential (E_{actual}) applied to the WE due to a high ohmic drop.[32]

$$E_{actual} = E_{app} - iR_{\Omega}$$

where E_{app} is the potential applied to the system and i is the current flowing between WE and RE. A current interruption technique[33−35] was used to calculate the value of iR_{Ω} in the 3.5 wt % NaCl solution, by applying galvanostatic pulses on glassy carbon WE. Potentials were monitored in response to currents of 100, 0, and −100 pA (Figure 1b). An average of 2.75 mV potential change was recorded consisting of capacitive and ohmic components,[35] when a current change of 100 pA occurred. As the current range measured in OI-SECCM was 100 pA in this work, the maximal iR_{Ω} was 2.75 mV, which can be negligible during experiments. Thus, the OI-SECCM setup can be used for a long-term scan. PDP measurements were performed at 2511 droplet landing locations, providing a wealth of information on multiple corrosion-related electrochemical processes. Figure 2a presents the reproducibility of 26 randomly selected PDP curves that are dispersed over 2511 locations. This demonstrates the stability of OI-SECCM measurements over the long time.

3.2. Grain-Orientation-Dependent Cathodic Current.

To visualize the dependence of cathodic process on grain orientations, cathodic currents were extracted from PDP curves at −1.3 V versus Ag/AgCl (Figure 2a), which were in the charge transfer controlled region (Figure S2). The cathodic current map was superimposed on grain boundaries as shown in Figure 2b, displaying a clear contrast between currents. This is consistent with the grain distribution as shown in Figure 2c. More specifically, the currents on {101} grains (green color in Figure 2c) are higher than others, indicating the enhanced cathodic reactions. To quantitatively present the dependence of corrosion processes on grain orientations, grains were categorized into three groups based on the misorientation angles of the planes relative to the three low-index grain families {001}, {101}, and {111} planes.

To spatially correspond the currents to grain orientations point by point, the grain orientation map was diluted (Figure S3a) to the same density as the cathodic current map. Because the misorientation angle is the rotation angle between two grains (Figure S3b), the smaller the misorientation angle, the closer the properties of the sample surface planes of two grains. We collected the grains with misorientation angles less than 20° to represent the three low index families, {001}, {101}, and {111}, as shown in Figures 2d and S3c. Currents on theses grains were extracted for the analyses of grain-orientation-dependent behaviors.

The cathodic currents grouped by grain orientations show a decreasing trend {101} > {001} > {111} (Figure 2e), which can be explained by the difference in surface energy (E^s). The surface energies of face centered cubic crystals calculated by

https://doi.org/10.1021/acsami.2c12813
ACS Appl. Mater. Interfaces 2022, 14, 47230−47236

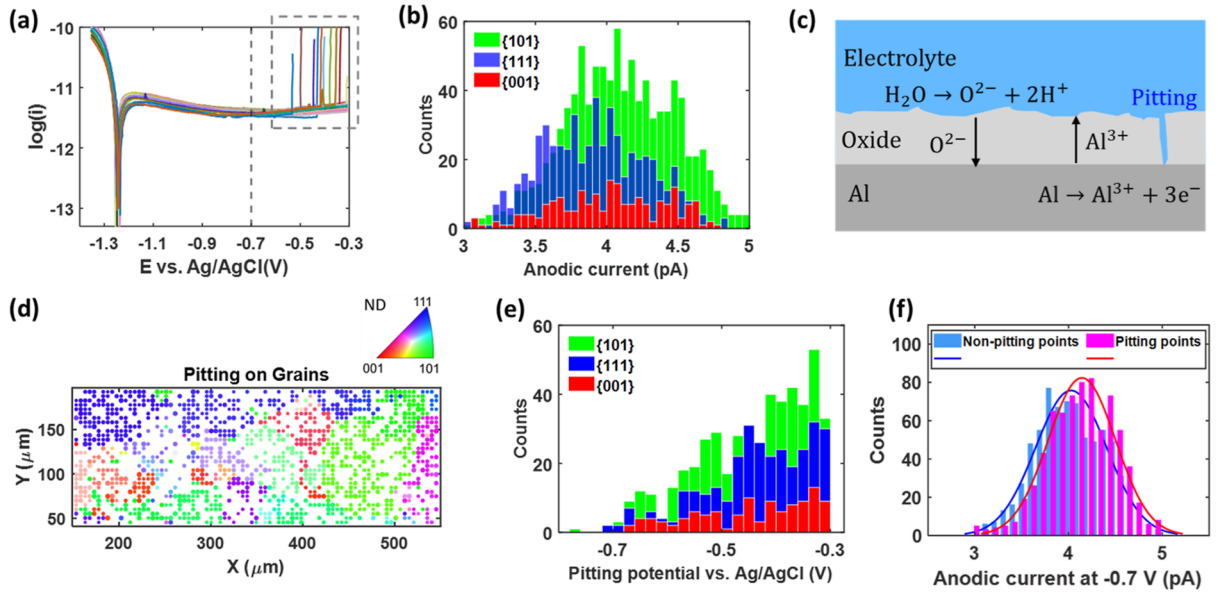

Figure 3. (a) Anodic currents extracted from PDP curves at −0.7 V vs Ag/AgCl, excluding the pitting peak current. (b) Statistical distribution of anodic currents on the three groups of grains {101}, {111}, and {001}. Currents were confined between 2.5 and 5.5 pA to remove the large currents on intermetallic particles. (c) Schematic of the migration of ions within the oxide film and the breakdown of oxide film that induces pitting. (d) Pitting occurred on different grains. (e) Statistical distribution of pitting occurring at different potentials on the three groups of grains {101}, {111}, and {001}. (f) Anodic current (at −0.7 V vs Ag/AgCl) distribution on the locations with and without pitting.

different methods vary, but the order for aluminum is consistent, {101} > {001} > {111}.[36−38] For example, the values given by the modified embedded atom method are $E_{\{101\}}^{s}$: 6.067 > $E_{\{001\}}^{s}$: 5.617 > $E_{\{111\}}^{s}$: 3.870 eV/nm^2,[39] whereas in the first-principles calculation method, the values are $E_{\{101\}}^{s}$: 6.813 > $E_{\{001\}}^{s}$: 6.756 > $E_{\{111\}}^{s}$: 5.869 eV/nm^2.[40] The order is in agreement with the theoretical prediction from the order of atomic planar density 0.177 < 0.250 < 0.289 atoms/r^2 (r is the radius of atom) for {101} < {001} < {111}. A loosely packed plane has less atoms and thus the less satisfied atomic bonds, resulting in a higher surface energy.[41,42] The higher surface energy plane can offer more sites for oxygen and water adsorption, thus facilitating the cathodic oxygen reduction and hydrogen evolution reactions.[43] This accounts for the higher cathodic currents on {101} grains. However, a macro study of single-crystal Al reported a higher rate of cathodic reactions on the {001} plane in 0.5 M NaCl.[16] The contradiction could stem from the difference in the materials and number of measurements. Because the current differences between grains are small, inadequate repetitions of measurements may not reflect the current trend. The advantage of SECCM is allowing multiple measurements on the same grain of a real polycrystalline sample, which can provide a statistical analysis for the current trend, ensuring the reliability of results.

3.3. Weak Correlation between Anodic Currents and Grain Orientations. Anodic currents were extracted from PDP curves at −0.7 V (Figure 3a) to represent the anodic corrosion process, Al dissolution. The anodic current distribution presents weak grain orientation dependence as shown in Figure 3b. {101} grains have the highest anodic currents, whereas anodic currents on {001} and {111} are in the same range between 3.0 and 4.8 pA. This could be due to the close atomic planar densities of {001} and {111}, which are 0.25 and 0.289 atoms/r^2, respectively, whereas {101} grains possess a much smaller planar density, 0.177 atoms/r^2, which facilitates the escape of Al atoms from bulk material.[44] In combination with the higher cathodic currents on the {101} grains, it can be inferred that the corrosion rate on {101} grains is higher than that on {001} and {111}.

Compared to the grain orientation, the surface oxide film may play a more important role in determining the magnitude of anodic current. The generation of anodic current involves Al oxidation at the metal-oxide interface, and the migration of Al^{3+} and O^{2-} through the oxide film (Figure 3c) under an electric field according to the Cabrera−Mott theory.[45−47] The thickness and structure of the oxide film affect the electric field strength and thus the migration rate of ions. It has been reported that the migration rate of ions within the oxide film limits the anodic process.[48,49] Therefore, the oxide film limits the anodic current and has a greater effect than the underlying crystal orientation. However, the relationship between the growth of the natural oxide film and grain orientation is still unclear, and most studies were performed under unrealistic conditions, such as high oxygen pressures.[2,50,51] The surface heterogeneity including the variations in the oxide film and grain boundaries could account for the wide statistical distribution of both cathodic and anodic currents (Figure S4a,b), which have shown to be independent of the misorientation angles relative to the three low index planes (Figure S4c,d).

3.4. No Correlation between Pitting and Grain Orientations. The breakdown of the oxide film exposed the underlying Al matrix to the electrolyte, giving rise to current transient peaks on PDP curves (Figure 3a), which represented pitting or metastable pitting as depicted in Figure 3c.[52−54]Figure 3d shows the distribution of pitting on grains in different orientations. On a PDP curve measured from negative to positive potentials, a more negative onset potential of pitting (pitting potential) indicates a higher pitting susceptibility,[53] suggesting a more defective oxide film structure. Therefore, the number of pitting locations was presented as a function of pitting potential and categorized

https://doi.org/10.1021/acsami.2c12813
ACS Appl. Mater. Interfaces 2022, 14, 47230−47236

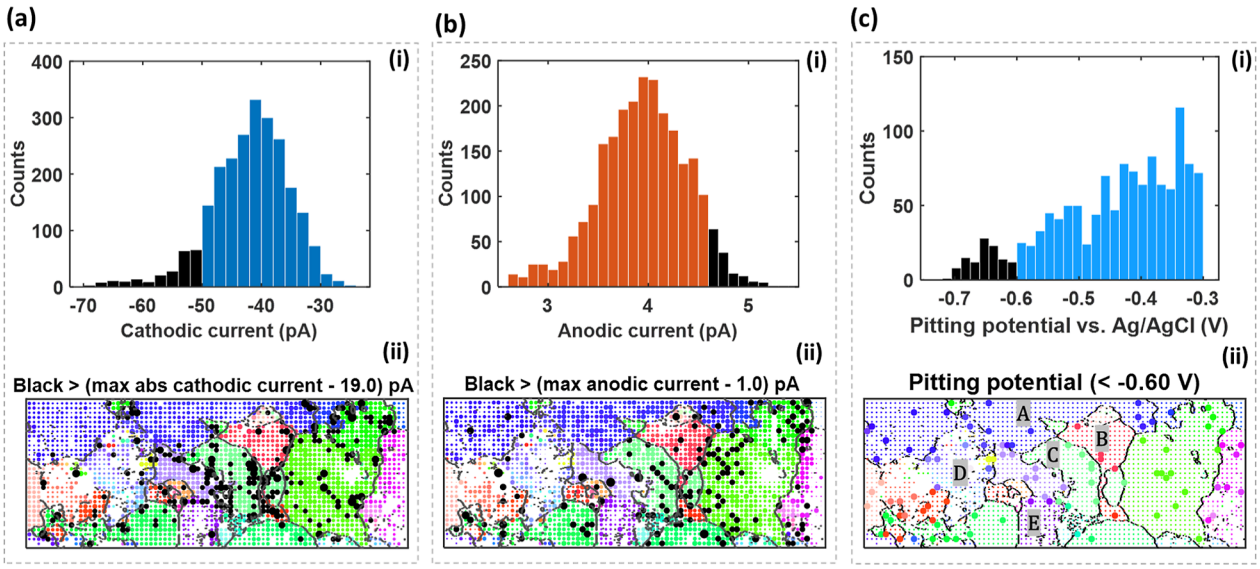

Figure 4. Histograms and maps of (a) cathodic currents at −1.3 V vs Ag/AgCl and (b) anodic currents at −0.7 V vs Ag/AgCl on different grains. Intermetallic particles were removed leaving empty points on the maps. The larger points on the maps indicate larger cathodic and anodic currents. The black points in (a-ii) and (b-ii) are values in black bins of the histograms (a-i) and (b-i). (c) Histogram of pitting occurring at different potentials (c-i). Black bins correspond to the pitting points (larger ones) more negative than −0.6 V vs Ag/AgCl on different grains in (c-ii).

into the three groups of {001}, {101}, and {111}. Figure 3e shows that pitting and grain orientations are not related in terms of both the number of pitting locations and pitting potential. It could be due to the dependence of pitting on the oxide film and imply that the relationship between the growth of the natural oxide film and grain orientation is weak.

H Krawiec and Szklarz reported that a high density of dislocations caused by plastic deformation affected the properties of the oxide film, leading to an increase in the pitting susceptibility, which was not influenced by grain orientations.[55] It implies that when the defectiveness of the oxide film is dominant, pitting will be independent of the underlying grain orientations. To check if the pitting locations indicate a more defective oxide film,[52] which can produce higher currents, the anodic currents at pitting and non-pitting locations are compared. Figure 3f shows a diminutive but observable trend that pitting locations tend to generate higher anodic currents, suggesting the correlation between the structure of the oxide film and pitting.

3.5. Enhanced Corrosion Processes at Grain Boundaries. Grain boundary is more prone to corrosion compared to the grain interior due to the microstructural heterogeneity[56,57] and second-phase precipitates,[58] such as $MgZn_2$ in 7xxx series alloys that dissolves as an anode relative to the adjacent Al matrix.[59,60] The high reactivity of grain boundaries was exhibited on OI-SECCM maps. Larger cathodic and anodic currents (Figure 4ai,bi: black bars) were highlighted as black points on OI-SECCM maps. Most of the large cathodic current points reside near boundaries (Figure 4aii), suggesting enhanced cathodic reactions at boundaries. This is because of the less dense atomic packing and higher energy of grain boundaries[61] that facilitates the oxygen reduction and hydrogen evolution reactions.[62] By contrast, the large anodic currents (black points in Figure 4bii) show a weak relation to grain boundaries. They tend to be on {101} grains (green), as discussed above.

To check if pitting preferentially occurred at grain boundaries, locations with pitting potentials more negative than −0.6 V versus Ag/AgCl are displayed in Figure 4c. −0.6 V is arbitrarily selected as a dividing line. At more positive potentials in PDP, pitting is easier to occur because of the large electric driving force but might not reflect the influence of surface structure. To stress the influence of the surface structural defectiveness on pitting, the locations with pitting negative than −0.6 V (Figure 4ci) were collected, exhibited as larger points on the map (Figure 4cii). On the grains labeled A−E, pitting exhibits a boundary preference. On other grains, however, pitting is irregularly distributed, which could be at the defective points of the grain interior. Due to the large grain size (as shown in Figure 2c), we used a 2 μm diameter micropipette with a 5 μm separation between droplet landings in order to map more grains. Although the diameter of micropipette is large relative to the nanoscale grain boundaries, we can still glimpse the distinctive properties of grain boundaries.

4. CONCLUSIONS

This work explored the effects of grain orientations on cathodic and anodic corrosion processes and pitting of a polycrystalline Al alloy sample. Numerous measurements were performed on each grain, enabling statistical analyses of electrochemical differences between grains. The cathodic currents exhibited a strong grain orientation dependence, decreasing in the order of {101} > {001} > {111}, inversely related to the atomic planar density. Larger cathodic currents were found in grain boundary regions, proving the enhanced cathodic reactions at grain boundaries. However, because the anodic corrosion processes are more dependent on the properties of the oxide film, the anodic currents and pitting did not show clear grain dependence. This work highlights the powerful capability of OI-SECCM in identifying microstructure-induced differences in corrosion processes and will facilitate the electrochemical study of grains of practical polycrystalline samples.

https://doi.org/10.1021/acsami.2c12813
ACS Appl. Mater. Interfaces 2022, 14, 47230−47236

■ ASSOCIATED CONTENT

Supporting Information

The Supporting Information is available free of charge at https://pubs.acs.org/doi/10.1021/acsami.2c12813.

Composition of Al alloy AA7075-T73; optical microscopic, SEM images, and energy-dispersive X-ray spectroscopy maps of the OI-SECCM scanned surface of Al alloy; cathodic charge transfer and diffusion controlled current regions on a Tafel plot; grain maps grouped by the misorientation angles; and maps and plots of the relationship between the current distributions and misorientations (PDF)

■ AUTHOR INFORMATION

Corresponding Authors

Alban Morel − *Automotive and Surface Transportation Research Centre, Division of Transportation and Manufacturing, National Research Council Canada, Aluminum Technology Center, Saguenay G7H 8C3 Quebec, Canada*; Email: Alban.Morel@cnrc-nrc.gc.ca

Danick Gallant − *Automotive and Surface Transportation Research Centre, Division of Transportation and Manufacturing, National Research Council Canada, Aluminum Technology Center, Saguenay G7H 8C3 Quebec, Canada*; Email: Danick.Gallant@cnrc-nrc.gc.ca

Janine Mauzeroll − *Department of Chemistry, McGill University, Montreal H3A 0B8 Quebec, Canada*; orcid.org/0000-0003-4752-7507; Email: janine.mauzeroll@mcgill.ca

Author

Yuanjiao Li − *Department of Chemistry, McGill University, Montreal H3A 0B8 Quebec, Canada*

Complete contact information is available at: https://pubs.acs.org/10.1021/acsami.2c12813

Author Contributions

All authors have given approval to the final version of the manuscript.

Notes

The authors declare no competing financial interest.

■ ACKNOWLEDGMENTS

This work was conducted as part of a project funded by the NRC's METALTec industrial research group, the Centre québécois de recherche et de développement de l'aluminium (CQRDA) as well as the Canadian Office for Energy Research and Development (OERD). The authors would like to acknowledge the METALTec industrial research group members and sponsors that supported this investigation and publication. We also thank Dr. Nicolas Brodush for the EBSD mapping and interpretation of EBSD data.

■ REFERENCES

(1) Ng, C. K.; Ngan, A. H. Precise Control of Nanohoneycomb Ordering over Anodic Aluminum Oxide of Square Centimeter Areas. *Chem. Mater.* **2011**, *23*, 5264−5268.

(2) Nguyen, L.; Hashimoto, T.; Zakharov, D. N.; Stach, E. A.; Rooney, A. P.; Berkels, B.; Thompson, G. E.; Haigh, S. J.; Burnett, T. L. Atomic-Scale Insights into the Oxidation of Aluminum. *ACS Appl. Mater. Interfaces* **2018**, *10*, 2230−2235.

(3) Holme, B.; Ljones, N.; Bakken, A.; Lunder, O.; Lein, J. E.; Vines, L.; Hauge, T.; Bauger, Ø.; Nisancioglu, K. Preferential Grain Etching of AlMgSi (Zn) Model Alloys. *J. Electrochem. Soc.* **2010**, *157*, C424−C427.

(4) Yuan, Y.; Zhang, D.; Zhang, F.; Yang, C.; Gan, Y. Crystallographic Orientation Dependence of Nanopattern Morphology and Size in Electropolished Polycrystalline and Monocrystalline Aluminum: An EBSD and SEM Study. *J. Electrochem. Soc.* **2020**, *167*, 113505.

(5) Liu, Q.; Juul Jensen, D.; Hansen, N. Effect of Grain Orientation on Deformation Structure in Cold-Rolled Polycrystalline Aluminium. *Acta Mater.* **1998**, *46*, 5819−5838.

(6) Stoudt, M. R.; Levine, L. E.; Creuziger, A.; Hubbard, J. B. The Fundamental Relationships between Grain Orientation, Deformation-Induced Surface Roughness and Strain Localization in an Aluminum Alloy. *Mater. Sci. Eng., A* **2011**, *530*, 107−116.

(7) Ma, Y.; Zhou, X.; Liao, Y.; Yi, Y.; Wu, H.; Wang, Z.; Huang, W. Localised Corrosion in AA 2099-T83 Aluminium-Lithium Alloy: The Role of Grain Orientation. *Corros. Sci.* **2016**, *107*, 41−48.

(8) Wang, S.; Wang, J. Effect of Grain Orientation on the Corrosion Behavior of Polycrystalline Alloy 690. *Corros. Sci.* **2014**, *85*, 183−192.

(9) Dong, S.; Chen, X.; La Plante, E. C.; Gussev, M.; Leonard, K.; Sant, G. Elucidating the Grain-Orientation Dependent Corrosion Rates of Austenitic Stainless Steels. *Mater. Des.* **2020**, *191*, 108583.

(10) Liu, M.; Qiu, D.; Zhao, M.-C.; Song, G.; Atrens, A. The Effect of Crystallographic Orientation on the Active Corrosion of Pure Magnesium. *Scripta Mater.* **2008**, *58*, 421−424.

(11) Song, G.-L.; Xu, Z. Crystal Orientation and Electrochemical Corrosion of Polycrystalline Mg. *Corros. Sci.* **2012**, *63*, 100−112.

(12) Seo, J. H.; Ryu, J. H.; Lee, D. N. Effects of Cathodic Polarization on the Pitting Behavior of Aluminum Single Crystals in Hydrochloric Acid Solution. *Mater. Sci. Forum* **2002**, *408-412*, 1037−1042.

(13) Yasuda, M.; Weinberg, F.; Tromans, D. Pitting Corrosion of Al and Al-Cu Single Crystals. *J. Electrochem. Soc.* **1990**, *137*, 3708−3715.

(14) Gartland, P. Adsorption of Oxygen on Clean Single Crystal Faces of Aluminium. *Surf. Sci.* **1977**, *62*, 183−196.

(15) Lee, S.; White, H. S. Dissolution of the Native Oxide Film on Polycrystalline and Single-Crystal Aluminum in NaCl Solutions. *J. Electrochem. Soc.* **2004**, *151*, B479−B483.

(16) Treacy, G. M.; Breslin, C. B. Electrochemical Studies on Single-Crystal Aluminium Surfaces. *Electrochim. Acta* **1998**, *43*, 1715−1720.

(17) Williams, C. G.; Edwards, M. A.; Colley, A. L.; Macpherson, J. V.; Unwin, P. R. Scanning Micropipet Contact Method for High-Resolution Imaging of Electrode Surface Redox Activity. *Anal. Chem.* **2009**, *81*, 2486−2495.

(18) Ebejer, N.; Schnippering, M.; Colburn, A. W.; Edwards, M. A.; Unwin, P. R. Localized High Resolution Electrochemistry and Multifunctional Imaging: Scanning Electrochemical Cell Microscopy. *Anal. Chem.* **2010**, *82*, 9141−9145.

(19) Yule, L. C.; Bentley, C. L.; West, G.; Shollock, B. A.; Unwin, P. R. Scanning Electrochemical Cell Microscopy: A Versatile Method for Highly Localised Corrosion Related Measurements on Metal Surfaces. *Electrochim. Acta* **2019**, *298*, 80−88.

(20) Yule, L. C.; Shkirskiy, V.; Aarons, J.; West, G.; Bentley, C. L.; Shollock, B. A.; Unwin, P. R. Nanoscale Active Sites for the Hydrogen Evolution Reaction on Low Carbon Steel. *J. Phys. Chem. C* **2019**, *123*, 24146−24155.

(21) Yule, L. C.; Shkirskiy, V.; Aarons, J.; West, G.; Shollock, B. A.; Bentley, C. L.; Unwin, P. R. Nanoscale Electrochemical Visualization of Grain-Dependent Anodic Iron Dissolution from Low Carbon Steel. *Electrochim. Acta* **2020**, *332*, 135267.

(22) Daviddi, E.; Shkirskiy, V.; Kirkman, P. M.; Robin, M. P.; Bentley, C. L.; Unwin, P. R. Nanoscale Electrochemistry in a Copper/Aqueous/Oil Three-Phase System: Surface Structure−Activity-Corrosion Potential Relationships. *Chem. Sci.* **2021**, *12*, 3055−3069.

(23) Li, Y.; Morel, A.; Gallant, D.; Mauzeroll, J. Oil-Immersed Scanning Micropipette Contact Method Enabling Long-term Corrosion Mapping. *Anal. Chem.* **2020**, *92*, 12415−12422.

(24) Shkirskiy, V.; Yule, L.; Daviddi, E.; Bentley, C.; Aarons, J.; West, G.; Unwin, P. Nanoscale Scanning Electrochemical Cell Microscopy and Correlative Surface Structural Analysis to Map Anodic and Cathodic Reactions on Polycrystalline Zn in Acid Media. *J. Electrochem. Soc.* **2020**, *167*, 041507.
(25) Li, Y.; Morel, A.; Gallant, D.; Mauzeroll, J. Ag^+ Interference from Ag/AgCl Wire Quasi-Reference Counter Electrode Inducing Corrosion Potential Shift in an Oil-Immersed Scanning Micropipette Contact Method Measurement. *Anal. Chem.* **2021**, *93*, 9657−9662.
(26) Habib, K.; Al-Muhanna, K.; Al-Sabti, F.; Al-Arbeed, A. In *Measurement of Oxide Barrier-Film Thickness of Al-Alloy by Electrochemical Impedance Spectroscopy at the Nanometre-Scale, Defect and Diffusion Forum*; Trans Tech Publications Ltd, 2007; Vol. *268*; pp 1−13.
(27) Nguyen, T.; Foley, R. The Chemical Nature of Aluminum Corrosion: III. the Dissolution Mechanism of Aluminum Oxide and Aluminum Powder in Various Electrolytes. *J. Electrochem. Soc.* **1980**, *127*, 2563−2566.
(28) Barlag, R.; Nyasulu, F.; Starr, R.; Silverman, J.; Arthasery, P.; McMills, L. A Student-Made Silver-Silver Chloride Reference Electrode for the General Chemistry Laboratory: ∼10 min Preparation. *J. Chem. Educ.* **2014**, *91*, 766−768.
(29) da Silva, E. T. S. G. n.; Miserere, S.; Kubota, L. T.; Merkoçi, A. Simple On-Plastic/Paper Inkjet-Printed Solid-State Ag/AgCl Pseudoreference Electrode. *Anal. Chem.* **2014**, *86*, 10531−10534.
(30) Andreatta, F.; Fedrizzi, L. The Use of the Electrochemical Micro-Cell for the Investigation of Corrosion Phenomena. *Electrochim. Acta* **2016**, *203*, 337−349.
(31) Bentley, C. L.; Perry, D.; Unwin, P. R. Stability and Placement of Ag/AgCl Quasi-Reference Counter Electrodes in Confined Electrochemical Cells. *Anal. Chem.* **2018**, *90*, 7700−7707.
(32) Myland, J. C.; Oldham, K. B. Uncompensated Resistance. 1. The Effect of Cell Geometry. *Anal. Chem.* **2000**, *72*, 3972−3980.
(33) Baruzzi, A.; Ühlken, J. Current Interruption Potentiostat for Elimination of the IR Drop in Four-Electrode Systems. *J. Electroanal. Chem.* **1990**, *282*, 267−273.
(34) Birbilis, N.; Padgett, B. N.; Buchheit, R. G. Limitations in Microelectrochemical Capillary Cell Testing and Transformation of Electrochemical Transients for Acquisition of Microcell Impedance Data. *Electrochim. Acta* **2005**, *50*, 3536−3544.
(35) Gandomi, Y. A.; Aaron, D.; Houser, J.; Daugherty, M.; Clement, J.; Pezeshki, A.; Ertugrul, T.; Moseley, D.; Mench, M. Critical Review—Experimental Diagnostics and Material Characterization Techniques Used on Redox Flow Batteries. *J. Electrochem. Soc.* **2018**, *165*, A970−A1010.
(36) Wen, Y.-N.; Zhang, J.-M. Surface Energy Calculation of the FCC Metals by using the MAEAM. *Solid State Commun.* **2007**, *144*, 163−167.
(37) Fu, B.; Liu, W.; Li, Z. Calculation of the Surface Energy of FCC-Metals with the Empirical Electron Surface Model. *Appl. Surf. Sci.* **2010**, *256*, 6899−6907.
(38) Jinlong, L.; Hongyun, L. Effect of Surface Burnishing on Texture and Corrosion Behavior of 2024 Aluminum Alloy. *Surf. Coat. Technol.* **2013**, *235*, 513−520.
(39) Baskes, M. I. Modified Embedded-Atom Potentials for Cubic Materials and Impurities. *Phys. Rev. B: Condens. Matter Mater. Phys.* **1992**, *46*, 2727−2742.
(40) Schöchlin, J.; Bohnen, K.; Ho, K. Structure and Dynamics at the Al (111)-Surface. *Surf. Sci.* **1995**, *324*, 113−121.
(41) Lüth, H.*Solid Surfaces, Interfaces and Thin Films*; Springer: Berlin, 2001; Vol. *4*.
(42) Song, G.-L.; Mishra, R.; Xu, Z. Crystallographic Orientation and Electrochemical Activity of AZ31 Mg Alloy. *Electrochem. Commun.* **2010**, *12*, 1009−1012.
(43) Dwivedi, D.; Lepková, K.; Becker, T. Carbon Steel Corrosion: a Review of Key Surface Properties and Characterization Methods. *RSC Adv.* **2017**, *7*, 4580−4610.
(44) Zhang, L.; Szpunar, J. A.; Dong, J.; Ojo, O. A.; Wang, X. Dependence of Crystallographic Orientation on Pitting Corrosion Behavior of Ni-Fe-Cr Alloy 028. *Metall. Mater. Trans. B* **2018**, *49*, 919−925.
(45) Cabrera, N.; Mott, N. Theory of Metal Oxidation. *Rep. Prog. Phys* **1949**, *12*, 163−184.
(46) Cai, N.; Zhou, G.; Müller, K.; Starr, D. E. Temperature and Pressure Dependent Mott Potentials and Their Influence on Self-Limiting Oxide Film Growth. *Appl. Phys. Lett.* **2012**, *101*, 171605.
(47) Verwey, E. Electrolytic Conduction of a Solid Insulator at High Fields the Formation of the Anodic Oxide Film on Aluminium. *Physica* **1935**, *2*, 1059−1063.
(48) Hasenay, D.; Šeruga, M. The Growth Kinetics and Properties of Potentiodynamically Formed Thin Oxide Films on Aluminium in Citric Acid Solutions. *J. Appl. Electrochem.* **2007**, *37*, 1001−1008.
(49) Zhou, H.; Chhin, D.; Morel, A.; Gallant, D.; Mauzeroll, J. Potentiodynamic Polarization Curves of AA7075 at High Scan Rates Interpreted using the High Field Model. *npj Mater. Degrad.* **2022**, *6*, 20.
(50) Martinson, C.; Flodström, S. Oxygen Adsorption on Aluminum Single Crystal Faces Studied by AES, XPS and LEED. *Surf. Sci.* **1979**, *80*, 306−316.
(51) Flötotto, D.; Wang, Z.; Jeurgens, L. P.; Mittemeijer, E. Intrinsic Stress Evolution during Amorphous Oxide Film Growth on Al Surfaces. *Appl. Phys. Lett.* **2014**, *104*, 091901.
(52) Szklarska-Smialowska, Z. Pitting Corrosion of Aluminum. *Corros. Sci.* **1999**, *41*, 1743−1767.
(53) Gupta, R.; Sukiman, N.; Cavanaugh, M.; Hinton, B.; Hutchinson, C.; Birbilis, N. Metastable Pitting Characteristics of Aluminium Alloys Measured using Current Transients during Potentiostatic Polarisation. *Electrochim. Acta* **2012**, *66*, 245−254.
(54) Natishan, P.; O'Grady, W. Chloride Ion Interactions with Oxide-Covered Aluminum Leading to Pitting Corrosion: a Review. *J. Electrochem. Soc.* **2014**, *161*, C421.
(55) Krawiec, H.; Szklarz, Z. Combining the Electrochemical Microcell Technique and the Electron Backscatter Diffraction Method to Study the Electrochemical Behaviour of Polycrystalline Aluminium in Sodium Chloride Solution. *Electrochim. Acta* **2016**, *203*, 426−438.
(56) Tucker, G. J.; McDowell, D. L. Non-Equilibrium Grain Boundary Structure and Inelastic Deformation using Atomistic Simulations. *Int. J. Plast.* **2011**, *27*, 841−857.
(57) Ye, W.; Kumar, P.; Misra, M.; Mushongera, L. T. Local Damage in Grain Boundary Stabilized Nanocrystalline Aluminum. *Mater. Lett.* **2021**, *300*, 130153.
(58) Galvele, J.; de De Micheli, S. Mechanism of Intergranular Corrosion of Al-Cu Alloys. *Corrosion Sci.* **1970**, *10*, 795−807.
(59) Ramgopal, T.; Gouma, P.; Frankel, G. Role of Grain-Boundary Precipitates and Solute-Depleted Zone on the Intergranular Corrosion of Aluminum Alloy 7150. *Corrosion* **2002**, *58*, 687−697.
(60) Sha, G.; Cerezo, A. Early-Stage Precipitation in Al−Zn−Mg−Cu Alloy (7050). *Acta Mater.* **2004**, *52*, 4503−4516.
(61) Rohrer, G. S. Grain Boundary Energy Anisotropy: a Review. *J. Mater. Sci.* **2011**, *46*, 5881−5895.
(62) Zhu, E.; Xue, W.; Wang, S.; Yan, X.; Zhou, J.; Liu, Y.; Cai, J.; Liu, E.; Jia, Q.; Duan, X.; Li, Y.; Heinz, H.; Huang, Y. Enhancement of Oxygen Reduction Reaction Activity by Grain Boundaries in Platinum Nanostructures. *Nano Res.* **2020**, *13*, 3310−3314.

https://doi.org/10.1021/acsami.2c12813
ACS Appl. Mater. Interfaces 2022, 14, 47230−47236